RESEARCH ARTICLE

A Novel Load Frequency Control Strategy for a Modern Power System by Considering State-Space Modeling and Stability Analysis

DUC-TUNG TRINH[ID]1, (Graduate Student Member, IEEE), **YUAN-KANG WU**[ID]1, (Member, IEEE), **AND MANH-HAI PHAM**[ID]2, (Member, IEEE)

[1]Department of Electrical Engineering, National Chung Cheng University, Chiayi 62102, Taiwan
[2]Department of Energy Technology, Electric Power University, Hanoi 10000, Vietnam

Corresponding author: Manh-Hai Pham (haipm@epu.edu.vn)

ABSTRACT The increasing integration of renewable energy sources (RESs) into the power system reduces system inertia, which presents substantial challenges for maintaining frequency stability. Existing studies have mainly focused on using the load frequency control method (LFC) to stabilize area frequency and tie-line power by optimizing the parameters of supplementary control for synchronous generators (SGs). However, these works primarily used simplified first-order transfer functions for wind turbines (WT), high-voltage direct current (HVDC), and battery energy storage systems (BESS). They neglected dynamic models and, importantly, the impact of control parameters in supplementary frequency control strategies on the stability of the studied system. Therefore, this study proposes a novel load frequency control strategy that coordinates the operation of WT, HVDC, and BESS in conjunction with traditional SGs to participate in frequency regulation. The proposed strategy develops a comprehensive state-space model that incorporates accurate models of WT, HVDC, BESS, and SGs, along with their supplementary control strategies. Then, the developed state-space model was utilized to investigate the impact of control parameters in the supplementary frequency control strategies of BESS, HVDC, and WT on system stability. As a result, this work yields a specific range of coefficients for supplementary strategies to improve stability in the studied system. Lastly, a two-area interconnected benchmark system is adopted to validate the effectiveness of the proposed strategy. Based on the suggested parameters, the results demonstrate that the proposed strategy ensures frequency stability with a high penetration of RESs into the power grid. Furthermore, the results indicate that incorporating diverse sources, such as HVDC, WT, and BESS, to support SGs in frequency regulation reduces the impacts of low system inertia. This approach leads to an improved frequency response not only in areas where disturbances occur but also in other regions, provided that tie-line power interchanges are maintained in balance.

INDEX TERMS Load frequency control (LFC), area control error (ACE), wind generation, droop control, HVDC, BESS.

I. INTRODUCTION

In modern power systems, the increasing penetration of renewable energy resources (RESs) has reduced the overall

The associate editor coordinating the review of this manuscript and approving it for publication was Fabio Mottola[ID].

system inertia. The reduced inertia yields the frequency stability to become more volatile and unpredictable. Contrary to traditional power plants, using power electronic-based RESs results in their decoupling from the power system, making them incapable of directly responding to any frequency disturbance in an AC system [1], [2]. Thus, the frequency

nadir (FN) could become lower. In addition, the rate of change of frequency (ROCOF) is a crucial measure for assessing the inertia of a power system, particularly in situations when the use of RESs is high [3]. ROCOF is becoming important in power systems due to the potential for a significant change in ROCOF, leading to trigger load-shedding controllers and even causing a blackout [4].

The load frequency control method (LFC) has been critical to guarantee the frequency stability and tie-line power interchanges within the desired limits in interconnected power systems [5], [6]. Typically, the area control error (ACE) is calculated by multiplying the area frequency bias by the frequency deviation and adding the net tie-line flow error. This ACE value is then utilized as the input for the load frequency controller, which aims to regulate both the ACE and the interconnection frequency deviation. To guarantee frequency stability and maintain balanced tie-line power, this paper proposes a new coordinated frequency control strategy for the LFC two-area system to enhance frequency stability and address the challenges of low inertia systems. A comprehensive state-space model describing the proposed LFC model is introduced, incorporating the frequency control strategies of battery energy storage systems (BESS), wind turbines (WT), high-voltage direct current (HVDC), and traditional synchronous generators (SG).

A. RELATED WORKS

Various linear and non-linear control methods have been devised to maintain the tie-line power deviation and frequency deviation within the expected range, such as proportional-integral (PI) [7], [8], and proportional-integral-derivative (PID) [9], [10], and PD–PID cascade controllers [11]. Nevertheless, the dynamic behavior of area frequency and tie-line power in the interconnected systems using traditional PI or PID controllers exhibit significant oscillations and extended settling periods due to constraints imposed by physical restrictions, uncertainties in the system, and changes in loading conditions. It is increasingly important to tackle the control challenges faced by contemporary power systems.

The fuzzy approach has been introduced to tackle this challenge [12], [13]. However, fuzzy techniques generally require extensive expert knowledge of the system and long learning processes.

Another method is to use optimal controls [14], [15]. Although optimal controls methods successfully satisfy the desired performance, the unknown disturbance inputs are assumed to be norm-bounded with pre-known upper limits. The authors in [16] and [17] proposed a robust control for LFC to consider some uncertainties inside a controlled system, but there are some limitations to its application, including the high-order model formulation and difficulties in choosing weight functions. On the other hand, the system parameters change with the growth of RESs, directly impacting the previously optimized supplementary control parameters. This change can lead to oscillations

when frequency events occur. Additionally, while adaptive controllers have been studied, their complexity has hindered widespread implementation.

Since there is a growing level of interconnections between asynchronous areas and a considerable distance between generation and load centers, HVDC technology emerges as a highly suitable solution to address these challenges. Therefore, the authors in [14], [18], [19], [20], and [21] proposed an integrated hybrid HVAC-HVDC system into the LFC model. The simplified model for HVDC links was represented by a first-order transfer function, incorporating a time constant and gain constant as described in [18], [19], and [20]. However, the HVDC simplified model did not support analytical or mathematical procedure and failed to consider any physical parameters, such as rated capacity, voltage level, converter impedances, and HVDC loading. A precise representation of the HVDC tie-line was suggested for analyzing the LFC model in [14] and [21]. The author in [22] suggested a virtual inertia approach using derivative control for the LFC model, which integrates the HVDC system with BESS. These studies in [14], [18], [19], [20], and [21] utilize the HVDC model to enhance the control parameter optimization for the LFC model. However, it is not included or represented in the LFC state-space modeling. Consequently, the impact of HVDC on system stability has not been examined.

The influence of wind power on the LFC of a power system was investigated in [12], [14], [17], [23], [24], [25], [26], and [27]. The state-space representation of the dynamic model for controlling the two-area LFC system was constructed in [23] and [24]. However, the state-space model does not include the wind turbine model. In addition, these studies only employed the state-space model to optimize the control parameters without using it to examine the stability of the system.

The introduction of a coordinating system with SG, BESS, and WT is presented in [12]. It can guarantee equilibrium in power transmission and frequency. However, the management of the state of charge (SOC) for BESS was not be considered. An LFC hybrid model integrating SG, WT, PV, BESS, and HVDC was proposed in [14], [17], [25], [26], and [27]. These models are applied to represent a high penetration of RES integrated into power systems nowadays. The results indicate that these proposed methods can can reduce the power flow error on the tie-line and enhance frequency stability. Nevertheless, the WT and PV are presented by simple first-order transfer functions. These transfer functions cannot provide an accurate dynamic response of RES in the LFC structure. In addition, the state-space representation of the dynamic model for managing the two-area LFC system was not designed to assess the stability of the suggested parameter control.

B. MAIN CONTRIBUTIONS

The literature analyses above are summarized in Table 1, which indicates that various controllers with different optimization strategies have been proposed for the LFC problem.

TABLE 1. A brief literature survey of load frequency control.

Ref. No	Controller Type	Number of Areas	Generation Source Type	Non-linearity Effect
[7]	PI	2	Thermal	GDB
[8]	PI	2	Thermal	—
[9]	PID	2-4	Thermal	GDB-GRC
[10]	PID	2-4	Thermal+Hydro	GDB-GRC
[11]	PD-PID	3	Thermal	GRC
[12]	Fuzzy-GPC	2	Thermal+BESS+WT	—
[13]	Fuzzy	3	Thermal	—
[14]	TIDF	2	Thermal+Hydro+SMES+WT+PV (WT+PV first-order TF)	GRC
[15]	SM	2	Thermal	—
[16]	PI	3	Diesel	—
[17]	DSFC	4	Diesel+BESS+WT+PV (WT+PV first-order TF)	GDB-GRC
[18]	Fuzzy-PID	2	Thermal+Hydro+Gas+HVDC	—
[19]	PI	2	Thermal+Hydro+HVDC	GRC
[20]	I	2	Thermal+HVDC	GRC
[21]	FHODFC	2	Thermal+HVDC	—
[22]	I	2	Thermal+HVDC	—
[23]	MPC	2-3	Gas+WT	GRC
[24]	I	2	Thermal+WT	—
[25]	CDM	2	Thermal+Hydro+Gas+HVDC+WT+PV (first-order TF)	GRC
[26]	I	2	Thermal+Hydro+WT	—
[27]	—	1	Diesel+BESS+WT	—

However, the majority of these studies utilized simplified first-order transfer functions for WT, BESS, and HVDC, with the purpose of establishing mathematical models to optimize the parameters of supplementary control for SGs. These works did not discuss about the load frequency control strategy that coordinates the operation of WT, HVDC, and BESS in conjunction with traditional SGs to participate in frequency regulation. Additionally, when considering a high ratio of wind power, the rotor speed of WTs should be managed and the effects of wind speed should be considered. A simplified first-order transfer function cannot represent the complete characteristics of a WT. Furthermore, BESS is a critical power source significantly contributing to frequency regulation. Consequently, an effective BESS operation should include SOC management.

The motivation of this work is to propose a comprehensive LFC strategy to enhance frequency stability and address the challenges of low inertia systems. The main contributions of this work are summarized as follows:

1) The proposed LFC strategy coordinates the operation of WT, HVDC, and BESS in conjunction with traditional SGs to participate in frequency regulation.

In this work, a simplified model of WT, capable of analyzing the frequency response in the initial stage following system disturbances, replaces traditional first-order transfer functions. Additionally, a BESS model with SOC management is used to enhance simulation accuracy in the studied system.

2) The state-space model is developed based on the differential equations describing the models of WT, HVDC, BESS, and SGs, along with their supplementary control strategies. Subsequently, the state-space model is utilized to investigate the impact of control parameters in the supplementary frequency control strategies of BESS, HVDC, and WT on system stability. As a result, this study provides a specific range of coefficients for supplementary control strategies to ensure the stability of the studied system.

3) A two-area interconnected benchmark system with a high wind power penetration is established to validate the proposed strategy and the recommended parameters. The results indicate a noticeable enhancement in frequency stability when the suggested approach is implemented.
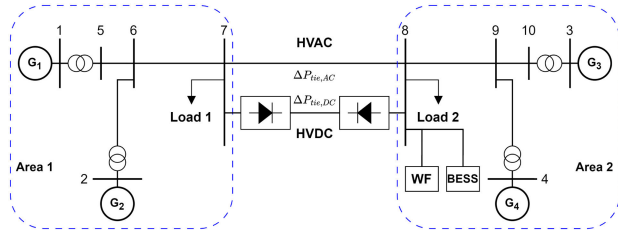
FIGURE 1. Single-line diagram of the studied two-area interconnected system.

C. PAPER ORGANIZATION

The remainder of this article is organized as follows: Section II provides a representation of the two-area interconnected system. Section III proposes the small-signal model of the studied system and the LFC strategy for frequency regulation coordinating WF, BESS, and HVDC for a two-area interconnected system. Section IV analyzes the stability of the state space model of the system. The simulation results are discussed in Section V. Finally, conclusions are drawn in Section VI.

II. MODELING OF TWO-AREA INTERCONNECTED SYSTEM

The diagram of the studied system, as presented in Fig. 1, comprises two areas: Area 1 includes two conventional hydraulic power stations (G1, G2), while Area 2 contains two reheat thermal power plants (G3, G4) [22], [28], [29]. The two areas are interconnected by hybrid HVAC and HVDC systems. To accurately analyze the frequency response in the context of power systems that significantly integrate RES, the wind farm (WF) is merged into bus 8 in Area 2. Furthermore, to efficiently address the disturbance caused by the growing RES and enhance the performance of the WF, the BESS is coordinated with the WF at bus 8 of Area 2.

A. CONVENTIONAL POWER PLANTS

In Area 1, there are two hydraulic power plants, referred to as G1 and G2. These power plants are simplified and represented by a transfer function that describes the hydraulic turbine and its governor considering transient droop compensation, as shown in Fig. 2 [28]. The power deviation of the governor x_1 can be expressed as

$$sx_1 = -\frac{1}{T_{G1}R_1}\Delta f_1 - \frac{1}{T_{G1}}x_1 + \frac{1}{T_{G1}}\Delta u_{g1}. \quad (1)$$

where R_1 is the droop coefficient of the governor, T_{G1} is the time delay of valve adjustment in the governor, and Δu_{g1} is the governor control signal. The power output of hydraulic turbine x_2 is given in (2).

$$sx_2 = -\frac{R_P}{T_{G1}R_TR_1}\Delta f_1 + \frac{R_P(T_{G1}-T_R)}{R_TT_RT_{G1}}x_1$$
$$- \frac{R_P}{R_TT_R}x_2 + \frac{R_P}{T_{G1}R_T}\Delta u_{g1}. \quad (2)$$

where R_T is temporary droop, R_P is the permanent droop and T_R denotes reset time. The output power deviation of the

hydraulic turbine is

$$s\Delta P_{SG1} = \frac{2R_P}{T_{G1}R_TR_1}\Delta f_1 + \frac{2R_P(T_R-T_{G1})}{R_TT_RT_{G1}}x_1$$
$$- \frac{2}{T_w}\Delta P_{SG1} + \left(\frac{2}{T_w}+\frac{2R_P}{R_TT_R}\right)x_2 + \frac{2R_P}{T_{G1}R_T}\Delta u_{g1}. \quad (3)$$

where T_w is referred to as the water starting time.

Using a methodology similar to Area 1, the transfer function of two thermal power plants is represented by the reheat steam turbine and its governor is shown in Fig. 2 [24], [28]. The power deviation of the governor x_3 can be mathematically represented as

$$sx_3 = -\frac{1}{R_2T_{G2}}\Delta f_2 - \frac{1}{T_{G2}}x_3 + \frac{1}{T_{G2}}\Delta u_{g2}. \quad (4)$$

where R_2 is the droop coefficient of the reheat governor, T_{G2} is the time delay of valve adjustment in the governor, and Δu_{g2} is the governor control signal. The power output of steam turbine x_4 is given in (5).

$$sx_4 = \frac{1}{T_{CH}}x_3 - \frac{1}{T_{CH}}x_4. \quad (5)$$

where T_{CH} is the time constant of main inlet volumes and steam chest. The output power deviation of the reheat steam turbine can be given in (6).

$$s\Delta P_{SG2} = -\frac{1}{T_{RH}}\Delta P_{SG2} + \frac{F_{HP}}{T_{CH}}x_3 + \frac{T_{CH}-F_{HP}}{T_{RH}T_{CH}}x_4. \quad (6)$$

where T_{RH} is the time constant of reheat, and F_{HP} fraction of total turbine power generated by high pressure sections. The characteristics for the hydraulic and thermal power plant models utilized in this study are presented in Section VI-A.

Practically, the change in power of thermal or hydropower plants can only occur at a specified maximum rate. That means each thermal or hydropower plant has the specified maximum allowable rate of change in the power output of a generator, typically measured in MW/min or %/min. Therefore, to ensure an accurate system frequency response due to physical limitations, the generation rate constraint (GRC) is considered in this work. The GRC plays a significant role in LFC model, it limits the speed at which generation can respond to frequency deviations. The GRC for the reheat thermal generation unit is set at a rate of 10 %/min (0.00167 pu/s) for both rising and decreasing rates. The GRC for hydraulic power generation is specified as 270 %/min (0.045 pu/s) for the growing rate and 360 %/min (0.06 pu/s) for the decreasing rate [19], [25].

B. AREA CONTROL ERROR

Considering the assistance provided by the HVDC system, the ACE signal for both Area 1 and Area 2 in Fig. 2 can be calculated as follows:

$$ACE_1 = B_1\Delta f_1 + \Delta P_{tie,eqv} + \Delta P_{DC} \quad (7)$$
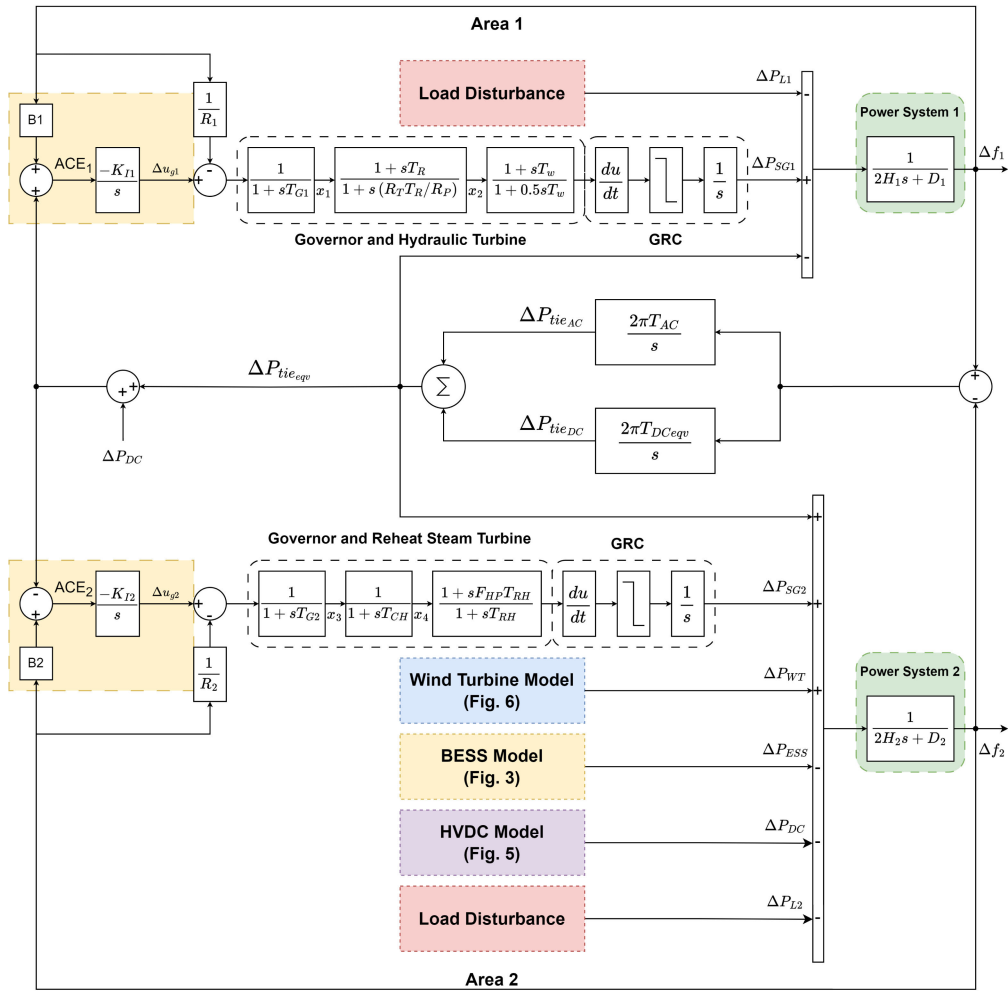$$ACE_2 = B_2\Delta f_2 - \Delta P_{tie,eqv} - \Delta P_{DC}. \quad (8)$$

FIGURE 2. LFC model of a two-area interconnected system in the presence of WT, HVDC, and BESS.

where B_1 and B_2 are the frequency deviation coefficients, ΔP_{DC} is the additional output power of the HVDC system, and $\Delta P_{tie,eqv}$ denotes the total tie-line power variation in a hybrid system.

C. TIE-LINE POWER MODEL
The tie-line power will be generated by hybrid HVAC-HVDC system. The total tie-line power variation in a hybrid system is given in (9).

$$s\Delta P_{tie,eqv} = 2\pi \left(T_{AC} + T_{DC} \right) \left(\Delta f_1 - \Delta f_2 \right). \qquad (9)$$

where T_{AC} is the AC synchronization coefficient of the AC line, and T_{DC} is the DC synchronization coefficient of the HVDC system. The comprehensive computation of the AC and DC synchronization coefficient is provided in section VI-B.

D. LOAD FREQUENCY CONTROL
The detailed transfer function model of the power system under study in Fig. 1 is depicted in Fig. 2. The frequency

deviation of the hybrid power system in Area 1 can be given in (10).

$$s\Delta f_1 = -\frac{D_1}{2H_1}\Delta f_1 + \frac{1}{2H_1}(\Delta P_{SG1} - \Delta P_{L1} - \Delta P_{tie,eqv}). \qquad (10)$$

where H_1 and D_1 are equivalent inertia constant and load damping in Area 1, respectively. Δf_1 represents the frequency deviation, ΔP_{SG1} is the output power of the hydraulic power plant, and ΔP_{L1} is the non-frequency-sensitive load change. Similarly, the frequency deviation in Area 2 can be expressed as

$$s\Delta f_2 = -\frac{D_2}{2H_2}\Delta f_2 + \frac{1}{2H_2}(\Delta P_{SG2} + \Delta P_{WT} - \Delta P_{ESS}$$
$$+ \Delta P_{tie,eqv} - \Delta P_{L2} - \Delta P_{DC}). \qquad (11)$$

where H_2 and D_2 denote equivalent inertia constant and load damping in Area 2, respectively. Δf_2 is the frequency deviation, ΔP_{SG2} is the output power of the thermal power plant, ΔP_{WT} is the output of the WF, ΔP_{ESS} is the output of
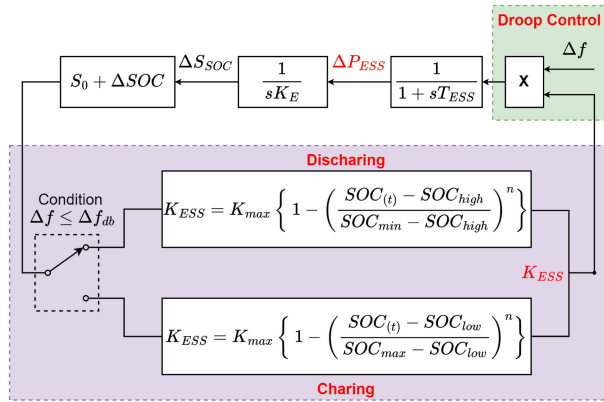
FIGURE 3. The control methodology BESS integrates management SOC.

FIGURE 4. BESS droop coefficient K_{ESS} with different n. (a) Discharging mode. (b) Charging mode.

the BESS, and ΔP_{L2} represents non-frequency-sensitive load change in Area 2.

E. BATTERY ENERGY STORAGE SYSTEM

The BESS is designed to respond to grid frequency deviations based on the droop algorithm. The output power of BESS (ΔP_{ESS}) can be yielded in (12).

$$s\Delta P_{ESS} = -\frac{1}{T_{ESS}}\Delta P_{ESS} + \frac{K_{ESS}}{T_{ESS}}\Delta f_2. \qquad (12)$$

where K_{ESS} is the droop coefficient of the BESS, and T_{ESS} is the time constant of the BESS. K_{ESS} is a function based on the state of SOC and the maximum droop coefficient K_{max}, which is determined as $K_{max} = \frac{1}{R_{ESS}}$. In discharging mode, $K_{ESS} = 0$ due to the output of the battery is equal to 0 when the SOC value is in the range $[0, SOC_{min}]$. In contrast, $K_{ESS} = K_{max}$ when the state of SOC in the range $[SOC_{high}, SOC_{full}]$ optimized output power of ESS. The $K_{ESS} \in (0, K_{max}]$ when the state of SOC in range $[SOC_{min}, SOC_{high}]$. The droop gain K_{ESS} in discharging mode when SOC in the interval $[SOC_{min}, SOC_{high}]$ is determined in (13) [30].

$$K_{ESS} = K_{max}\left\{1 - \left(\frac{SOC_{(t)} - SOC_{high}}{SOC_{min} - SOC_{high}}\right)^n\right\} \qquad (13)$$

Contrary to droop gain in discharging mode, if the SOC value in the range $[0, SOC_{low}]$, the battery need to charge maximum power if which can, we have $K_{ESS} = K_{max}$. When the SOC value is in the range $[SOC_{max}, SOC_{full}]$, the battery do not need charging, we have $K_{ESS} = 0$. The $K_{ESS} \in [K_{max}, 0)$ when the state of SOC in range $[SOC_{low}, SOC_{max}]$. The droop gain K_{ESS} in charging mode when SOC in the interval $[SOC_{low}, SOC_{max}]$ is determined in (14).

$$K_{ESS} = K_{max}\left\{1 - \left(\frac{SOC_{(t)} - SOC_{low}}{SOC_{max} - SOC_{low}}\right)^n\right\} \qquad (14)$$

A comprehensive strategy that adjusts the output active power of BESS and manages SOC can be summarized in Fig. 3. The relationship between SOC and droop coefficient K_{ESS} in charging and discharging mode with different coefficient n is depicted in Fig. 4.
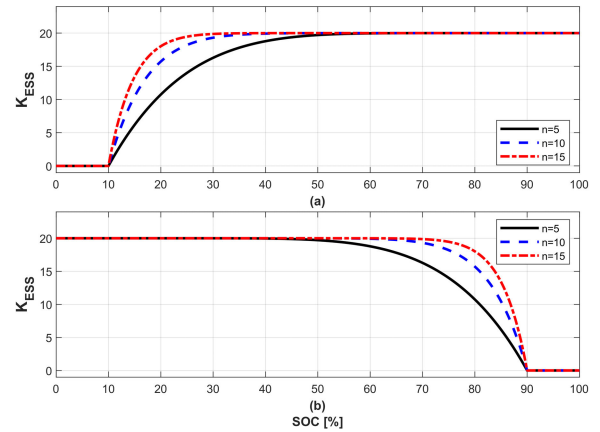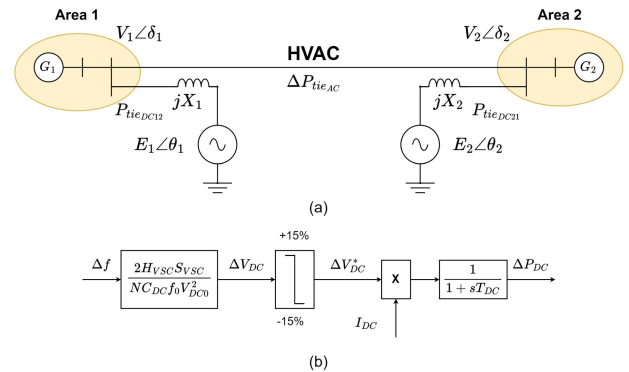

FIGURE 5. Schematic diagram of the interconnected two-area power system considering a hybrid HVAC-HVDC and INEC strategy.

F. HVDC SYSTEM

The interconnected two-area power system considering a hybrid HVAC-HVDC system has been shown in Fig. 1. According to [14] and [21], HVDC system can be modeled as a series composition of two voltage sources E_1, E_2, and their corresponding phase angles are θ_1 and θ_2, respectively. The equivalent two-area power system can be represented in Fig. 5(a). The relationship between the variations in the frequency of interconnected areas and the deviations in the power of the HVDC link is defined by (15) [21].

$$\Delta P_{tie DC12}(s) = \frac{2\pi T_{DC}}{s}(\Delta f_1(s) - \Delta f_2(s)). \qquad (15)$$

where $T_{DC} = T_{DC12}T_{DC21}/(T_{DC12} + T_{DC21})$ denotes the HVDC equivalent synchronization coefficient. T_{DC12} and T_{DC21} are the converter AC/DC synchronizing coefficient.

The inertia emulation control strategy (INEC) strategy harnesses energy stored in HVDC-link capacitors to provide the frequency regulation that can be obtained as follows [21]:

$$\Delta V_{DC} = \frac{2H_{VSC}S_{VSC}}{NC_{DC}f_0V_{DC0}^2}\Delta f. \qquad (16)$$
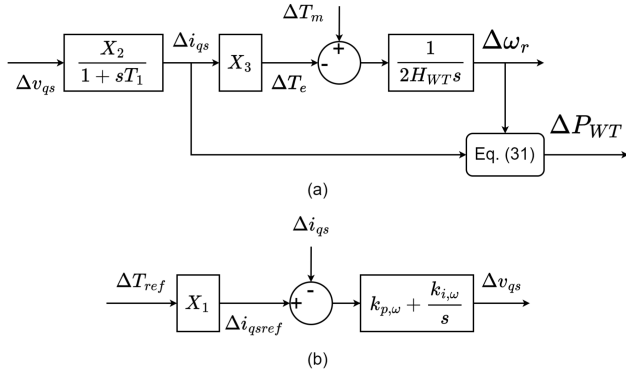
FIGURE 6. A simplified model for the PMSG-based WT for frequency studies.

FIGURE 7. WT power-speed characteristics and maximum power point operation.

where H_{VSC} is the inertia time constant of HVDC, S_{VSC} is the rated power capacity of VSC inverters, f_0 refers to the nominal frequency, V_{DC0} denotes rated DC voltage, N represents the number of capacitors in the HVDC link, and C_{DC} is the DC capacitance.

The voltage reference expression in (16) directly indicates that the voltage deviation ΔV_{DC} links with the power system's frequency deviations Δf. Fig. 5(b) illustrates the comprehensive transfer function block diagram of the DVIC, which is used to harness stored energy from the HVDC system.

G. WIND POWER GENERATION

A simplified model has been demonstrated to be capable of analyzing the frequency response of the permanent magnet synchronous generator (PMSG)-based WT in the initial seconds following system disturbances [31], [32], [33]. It is crucial to underscore that this model is valid for a short period after a disturbance and is employed in the frequency analysis. This simplified model is depicted in Fig. 6 for the PMSG-based WT and described by the following state equations [31], [32], [33]:

$$s\Delta i_{qs} = -\frac{1}{T_1}\Delta i_{qs} + \frac{X_2}{T_1}\Delta v_{qs}. \tag{17}$$

$$s\Delta \omega_r = -\frac{X_3}{2H_{WT}}\Delta i_{qs} + \frac{1}{2H_{WT}}\Delta T_m. \tag{18}$$

$$\Delta v_{qs} = \left(\Delta T_{ref}X_1 - \Delta i_{qs}\right)\left(k_{p\omega} + \frac{k_{i\omega}}{s}\right). \tag{19}$$

where i_{qs}, v_{qs}, $\Delta\omega$, H_{WT}, and ΔT_m are stator quadrature current, stator quadrature voltage, deviation rotational speed, inertia constant of WT, and aerodynamic torque, respectively. All parameters in these state equations are defined in Table 2, where L_m, L_{lr}, and L_{ls} are the magnetizing inductance, rotor inductance, and stator inductance, respectively. R_s is the stator resistances. The mechanical power P_m extracted from wind energy is given in (20).

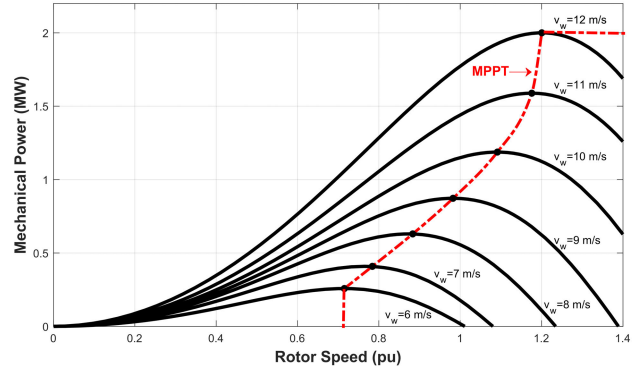$$P_m = \frac{\rho}{2}\pi R^2 v_\omega^3 C_p(\lambda, \beta). \tag{20}$$

TABLE 2. PMSG-based WT simplified model parameters and specifications [32], [33].

Simplified Model Parameters			
X_1	X_2	X_3	T_1
$\frac{L_{lr}+L_m}{L_m}$	$\frac{1}{R_s}$	$\frac{L_m}{L_{lr}+L_m}$	$\frac{L_m+L_{ls}}{\omega_s R_s}$

Specifications	
Parameter	Value
Stator Resistance R_s	0.00488 (pu)
Stator Inductance L_{ls}	0.09241 (pu)
Rotor Inductance L_{lr}	0.09955 (pu)
Magnetizing Inductance L_m	3.95279 (pu)
Lumped Inertia Constant H_{WT}	4.5

where ρ is the air density, R is the rotor blade radius, v_ω is the wind speed, λ is the tip speed ratio, β is the pitch angle, and C_p is the power coefficient. The tip speed ratio can be determined as follows:

$$\lambda = \frac{\omega_r R}{v_\omega}. \tag{21}$$

The power coefficient C_p is a function between λ and β, which can be defined in (22) [27].

$$C_p(\lambda, \beta) = 0.22\left(\frac{116}{\lambda_i} - 0.4\beta - 5\right)e^{-12.5/\lambda_i}. \tag{22}$$

$$\frac{1}{\lambda_i} = \frac{1}{\lambda_{opt} + 0.08\beta} - \frac{0.035}{\beta^3 + 1}. \tag{23}$$

where λ_{opt} is the optimal tip speed ratio. The pitch angle is set to $\beta = 0$ to maximize the output power of WT in this work. Hence, C_p is the function of λ only and reaches the maximum $C_{p,max}$ at the optimal tip speed ratio λ_{opt} as described in (24).

$$P_{mppt} = \frac{\pi\rho R^5 C_{p,max}}{2\lambda_{opt}^3}\omega_r^3 = k_{opt}\omega_r^3. \tag{24}$$

where P_{mppt} is the active power reference determined by the MPPT algorithm, and k_{opt} is the MPPT curve coefficient. The operation characteristics of WT as a function of rotor speed ω_r and the mechanical power P_ω are presented in

TABLE 3. The lookup table of each point on the power-speed curve.

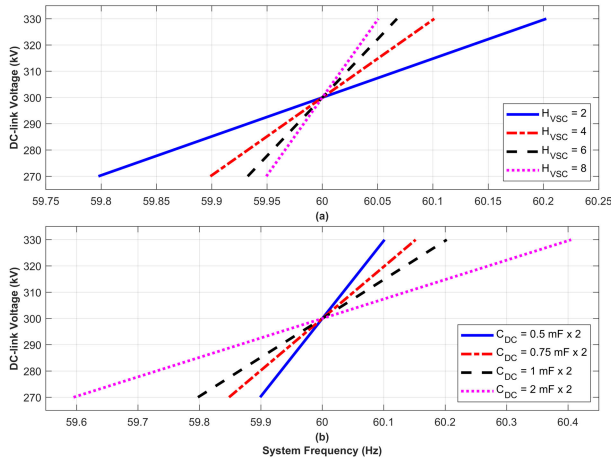| Points	Wind speed (m/s)	Mechanical Power (MW)
1	6	0.2578
2	7	0.4088
3	8	0.6298
4	9	0.8725
5	10	1.1874
6	11	1.5886
7	12	2.0
8	13	2.0
9	14	2.0

FIGURE 8. The relationship between system frequency and DC voltage V_{DC} for different values. (a) Varying H_{VSC} with total capacitance 0.5 mF x 2. (b) Varying C_{DC} with $H_{VSC} = 4$.

Fig. 7, while the corresponding relationship between them is shown in Table 3. The linearized expression for the MPPT algorithm in (24) concerning the rotor operating point ω_{r0} can be described as follows:

$$\Delta P_{\text{mppt}} = 3\,k_{opt}\omega_{r0}^2 \Delta\omega_r. \quad (25)$$

In this study, the WT utilizes the droop strategy to provide its ability to contribute to frequency regulation. The droop control strategy output power is proportional to the system frequency deviation Δf, which can be given in (26).

$$\Delta P_D = -K_D \Delta f. \quad (26)$$

where K_D is the droop coefficient. Under normal conditions, a WT will use the MPPT algorithm to control active power delivery to the grid. The power deviation reference integrates droop controls during an FS state, as presented in (27).

$$\Delta P_{ref} = \Delta P_{mppt} + \Delta P_D = 3k_{\text{opt}}\omega_{r0}^2\Delta\omega_r - K_D\Delta f_2. \quad (27)$$

The mechanical torque $\Delta T_m = \frac{P_m}{\omega_r}$ is linearized at the operation point and is given as follows [27], [32], and [33].

$$\Delta T_m = \tau_1 \Delta\omega_r + \tau_2 \Delta v_\omega. \quad (28)$$

where $\tau_1 = \frac{\partial T_m}{\partial \omega_r}$ is the intrinsic rotor damping, and $\tau_2 = \frac{\partial T_m}{\partial v_\omega}$ is a perturbation caused by the variations in wind speed.

The details of τ_1 and τ_2 are thoroughly discussed in [27]. Substituting (28) into (18), the deviation rotational speed is rewritten in (31).

$$s\Delta\omega_r = -\frac{X_3}{2H_{WT}}\Delta i_{qs} + \frac{\tau_1}{2H_{WT}}\Delta\omega_r + \frac{\tau_2}{2H_{WT}}\Delta v_\omega. \quad (29)$$

The WT output power based on the state variable i_{qs} and ω_r is given in (30) [23], [33].

$$P_{WT} = -X_3 i_{qs}\omega_r. \quad (30)$$

The Taylor series expansion of a Wind Energy Conversion System (WECS) is estimated around its Maximum Power Point (MPP), as given in (31).

$$\Delta P_{WT} = -X_3\omega_{r0}\Delta i_{qs} - X_3 i_{qs0}\Delta\omega_r. \quad (31)$$

where ω_{r0} and i_{qs0} are the rotor speed at the MPPT point and GSC current, respectively.

III. THE PROPOSED MODEL

A. THE PROPOSED COORDINATED FREQUENCY REGULATION STRATEGY FOR THE LFC MODEL

Fig. 2 presents the LFC two-area interconnected system model, as seen in Fig. 1, and an extensive explanation of the control strategies for SGs, BESS, HVDC, and WT. By implementing the INEC strategy in (15) to modify DC voltage, the energy stored in HVDC-link capacitors is harnessed to improve system inertia. The output power of HVDC ΔP_{DC} can be given in (32).

$$\Delta P_{DC} = \frac{2H_{VSC}S_{VSC}I_{DC}}{NC_{DC}f_0V_{DC0}^2}\Delta f_2. \quad (32)$$

where ΔP_{DC} is DC power flow through the system. The time constant H_{VSC} can be presented in (33).

$$H_{VSC} = \frac{NC_{DC}f_0V_{DC0}\Delta V_{DC}}{2S_{VSC}\Delta f}. \quad (33)$$

In practice, the maximum allowable DC voltage deviation is ± 0.1 p.u [34]. Therefore, this study set the limitation of DC voltage reference in the interval [0.9, 1.1] p.u. To evaluate the effect of DC voltage and system frequency on the emulated time constant H_{VSC}, their trends containing different H_{VSC} values for variable f and V_{DC} are drawn in Fig. 8. It can be seen from Fig. 8(a) that a larger H_{VSC} leads to a larger V_{DC} for a given f, as a larger H_{VSC} means more significant energy is exchanged with the grid when the grid frequency changes. Furthermore, the effect of different values of C_{DC} with fixed H_{VSC} is investigated in Fig. 8(b). It is shown that the DC-link voltage changes within a smaller range with a larger capacitance compared to the case with a smaller capacitance.

To guarantee a precise frequency response of the system despite physical limitations, the GRC is considered during SG operation. Furthermore, the droop method, rotor speed, and MPPT algorithm are incorporated into the advanced WT control strategy to generate additional power at varying wind speeds. On the other hand, the adaptive strategy and

integrated SOC management are utilized to regulate the BESS output power. The rated power of BESS is 50 [MW] in this work. The energy rating of BESS is determined based on the duration of primary frequency regulation (PFR) as specified in the grid code. Assuming BESS can provide PFR at a rated power of around 15 minutes [35], and charging efficiency equals discharging efficiency of 0.85 [3], [36], then the rated energy of BESS is yielded as [36]:

$$E_{BESS} = \frac{\int_t^{t+900} P_{BESS}(t)\sqrt{\eta_c}dt}{3600} + \frac{\int_t^{t+900} P_{BESS}(t)\,dt}{3600\sqrt{\eta_d}}.$$

(34a)

$$E_{BESS} = \frac{900*50*\sqrt{0.85}}{3600} + \frac{900*50}{3600\sqrt{0.85}} \cong 24\,[\text{MWh}].$$

(34b)

The rating of BESS is designed as 50 MW/24 MWh in this work.

B. THE PROPOSED STATE-SPACE OF LFC THE TWO-AREA INTERCONNECTED SYSTEM

To perform a detailed analysis of the two-area power system, a complete state-space model of the studied system is expressed as follows:

$$\dot{x} = Ax + B_1u + B_2\omega.$$

(35)

where x refers to the state variable, u, and ω are the control and disturbance variables, respectively. A denoted the state matrix, B_1 and B_2 are the control and disturbance matrix, respectively. The 15 state variables have been considered for the state-space analysis given as follows:

$$x = \begin{bmatrix} \Delta f_1, & \Delta P_{SG1}, & x_1, & x_2, & \Delta P_{ESS}, \\ \Delta P_{tie,eqv}, & \Delta f_2, & \Delta P_{SG2}, & x_3, \\ x_4, & x_5, & x_6, \\ \Delta\omega_r, & \Delta i_{qs}, & \Delta v_{qs} \end{bmatrix}^T.$$

(36)

where $x_5 = \int ACE_1$ and $x_6 = \int ACE_2$. The specific parameters of the system matrix are provided in section VI-C. The disturbances variables can be given as follows:

$$\omega = \begin{bmatrix} \Delta P_{L1} & \Delta P_{L2} & \Delta v_\omega \end{bmatrix}^T.$$

(37)

The control variables can be yielded in (38).

$$u = \begin{bmatrix} \Delta u_{g1} & \Delta u_{g2} \end{bmatrix}^T.$$

(38)

IV. SYSTEM ANALYSIS

To investigate the effects of frequency control strategies implemented by HVDC, BESS, and WT on the system under study, this section focuses on three primary aspects. The first part examines the impact of BESS droop gain on the stability of the system. The second part evaluates the system stability by analyzing the influence of the WT at different wind speeds and the variable droop coefficient. Finally, the impact of the DC capacitance on the system stability is considered.

TABLE 4. Eigenvalues and participation factor analysis.

Mode	Eigenvalue	Associated States	PF
λ_1	$0.00 + 0.00i$	——	——
λ_2	$0.00 + 0.00i$	——	——
λ_3	$-18.643 + 0.00i$	$x_4, x_6,$ $\Delta P_{ESS}, x_3$	0.489, 0.209, 0.125, 0.116
λ_4	$-5.825 + 0.00i$	$\Delta P_{SG1}, \Delta f_1,$ x_5, x_4	0.944, 0.025, 0.021, 0.005
λ_5	$-6.209 + 0.00i$	$x_3, \Delta P_{ESS},$ $\Delta P_{SG2}, x_4$	0.457, 0.221, 0.150, 0.078
λ_6	$-1.734 + 1.749i$	$x_4, x_3,$ $x_6, \Delta P_{SG2}$	0.449, 0.260, 0.152, 0.100
λ_7	$-1.734 + -1.749i$	$x_3, \Delta P_{ESS},$ $\Delta P_{SG2}, x_4$	0.431, 0.275, 0.166, 0.063
λ_8	$-0.052 + 0.783i$	$\Delta i_{qs}, x_3,$ $x_6, \Delta P_{SG2}$	0.544, 0.159, 0.059, 0.053
λ_9	$-0.052 + -0.783i$	$\Delta P_{ESS}, x_3,$ $\Delta i_{qs}, \Delta P_{SG2}$	0.557, 0.143, 0.100, 0.048
λ_{10}	$-0.870 + 0.000i$	$\Delta P_{SG1}, x_5,$ $x_3, \Delta P_{tie}$	0.839, 0.089, 0.028, 0.012
λ_{11}	$-0.220 + 0.452i$	ΔP_{SG1}	1.000
λ_{12}	$-0.220 - 0.452i$	ΔP_{SG1}	1.000
λ_{13}	$-0.024 + 0.000i$	$x_5, \Delta P_{SG2},$ x_3, x_6	0.349, 0.241, 0.210, 0.129
λ_{14}	$-0.326 + 0.000i$	$x_3, \Delta P_{SG2},$ x_6, x_5	0.714, 0.195, 0.032, 0.027
λ_{15}	$-0.564 + 0.000i$	$x_3, \Delta v_{qs},$ $\Delta i_{qs}, \Delta P_{SG2}$	0.612, 0.158, 0.087, 0.046

The state space model given in (35) has 15 eigenvalues, denoted by λ_i, $i = 1, \ldots, 15$. For stability analysis, fixed $K_{ESS} = 10$ and wind speed $v_\omega = 10.5$ m/s is considered. To validate the effectiveness of system parameters and highlight their robustness against operation point change, the participation factor analysis is performed to determine the participation of the state variable in modes of eigenvalue λ_i, shown in Table 4. The eigenvalues are in the left half-plane of the complex plane, indicating that the system is stable with the control parameters and system parameters used. The extensive investigation of system stability with varying K_{ESS} in the operation range will be discussed in Section IV-A. Similarly, in Section IV-B, the system stability examination with K_D and wind speed in different values will be considered. Furthermore, section IV-C investigates its effect on system stability in terms of energy stored in the DC-link capacitor.

A. SYSTEM STABILITY ANALYSIS WITH VARIATION IN BESS DROOP COEFFICIENT

In this section, the dynamic effects of varying BESS droop K_{ESS} on frequency control in the studied system is analyzed. The main objective is to evaluate system stability when the K_{ESS} operates in the interval $[0, K_{max}]$.
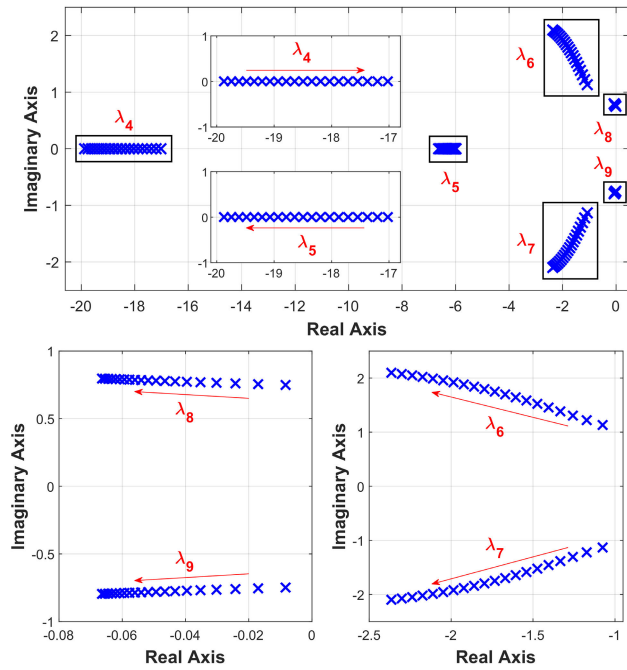
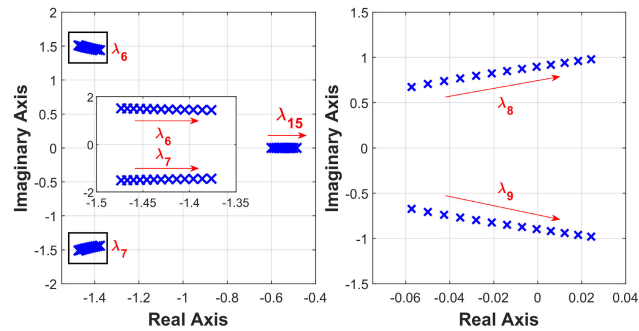**FIGURE 9.** The dominant mode of the BESS strategy when K_{ESS} increases from 1 to 20.

FIGURE 10. The dominant mode of the WT strategy when K_D increases from 1 to 13.

The system eigenvalue trajectory considering variation in K_{ESS} from 1 to 20 is depicted in Fig. 9. The results indicate that system stability is ensured when all eigenvalues affected by changes in K_{ESS} are located on the left of the imaginary axis. As K_{ESS} increases, λ_{6-7} and λ_{8-9} move to the left on the s-plane, improving the dynamic response due to the damping and speed response increase. Similarly, when K_{ESS} increases, λ_5 moves away from the imaginary axis and increases the response speed of the system. In addition, λ_4 moves toward the right and reduces the response speed. In summary, the results indicate that the BESS strategy with varying K_{ESS} in the operation range $[0, K_{max}]$ can maintain system stability.

B. SYSTEM STABILITY ANALYSIS WITH VARIATION CONDITIONS IN WT

The increased wind power penetration in the grid necessitates its involvement in frequency regulation. Therefore, it is
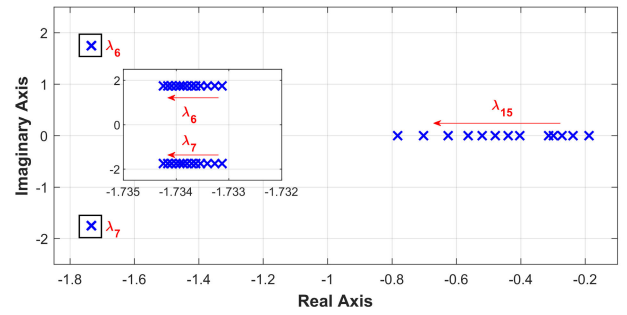

FIGURE 11. The dominant mode of the WT strategy when wind speed v_ω increases from 5 to 12 m/s.

essential to evaluate the control parameters within each of those strategies. In addition, system stability needs to be evaluated at different wind speeds. Therefore, the effects of control parameters and different wind speeds on system stability will be investigated in this section.

As shown in Fig. 10, once K_D increases, λ_{6-7} move toward the right of the imaginary axis, and both the response speed and damping ratio of the system decrease. Similarly, as K_D increases, λ_{15} also move toward the right and decreases the response speed. Concerning the eigenvalue λ_{8-9}, it is evident that the system becomes unstable when the dominating eigenvalues are in the right half-plane of the complex plane, which occurs when $K_D > 10$. The eigenvalue λ_{8-9} approaches the imaginary axis and intersects the real axis when K_D exceeds 10. Thus, the value of K_D less than 10 is chosen to guarantee the stability of the system.

Another comparison regarding the eigenvalue of the systems with different wind speeds is presented in Fig. 11. It can be observed that eigenvalue λ_{15} moves away from the imaginary axis with increasing wind speed 5 to 12 m/s, which improves the system stability. As wind speed increases, λ_{6-7} moves away from the imaginary axis, and both the response speed and damping ratio of the system increase. Overall, the system stability will be ensured within the operational range of wind speed with system parameters and control parameters used.

High penetration of wind power in power grids reduces system inertia, leading to more unpredictable frequency stability. Therefore, the change in WT inertia H_{WT} will be considered to evaluate the effects of high penetration of WT on system stability. Fig. 12 depicts the system eigenvalue trajectory considering variation in H_{WT} from 1 to 4. As shown in Fig. 12, when H_{WT} increases, λ_{15} moves toward the right of the imaginary axis. As H_{WT} increases, the eigenvalues λ_{8-9} move away from the imaginary axis and improve the dynamic response. Therefore, it can be concluded that the increasing inertia of WTs improves response speed and more stable system behavior through trajectories of λ_{14-15}.

C. SYSTEM STABILITY ANALYSIS CONSIDERING HVDC

Besides BESS and WTs, the HVDC system serves as another resource for frequency control, aiding the SGs in maintaining system stability. Therefore, the HVDC should
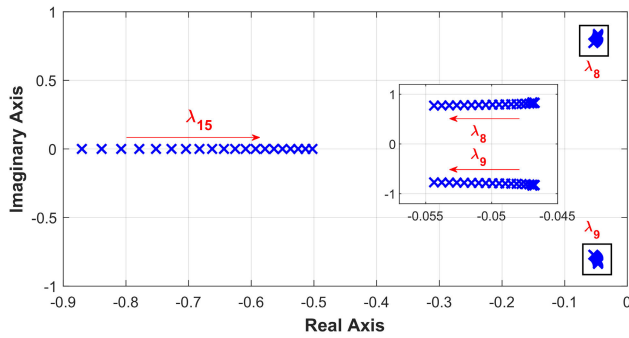
FIGURE 12. The dominant mode of the WT strategy when WT inertia H_{WT} increases from 1 to 4.

TABLE 5. Eigenvalues for different DC capacitance.

Mode	$C_{DC} = 0.5$ mF	$C_{DC} = 5$ mF	$C_{DC} = 50$ mF
λ_1	$0 + 0i$	$0 + 0i$	$0 + 0i$
λ_2	$0 + 0i$	$0 + 0i$	$0 + 0i$
λ_3	$-18.643 + 0i$	$-18.644 + 0i$	$-18.645 + 0i$
λ_4	$-5.825 + 0i$	$-5.825 + 0i$	$-5.825 + 0i$
λ_5	$-6.209 + 0i$	$-6.206 + 0i$	$-6.206 + 0i$
λ_6	$-1.734 + 1.749i$	$-1.725 + 1.743i$	$-1.724 + 1.743i$
λ_7	$-1.734 - 1.749i$	$-1.725 - 1.743i$	$-1.724 - 1.743i$
λ_8	$-0.052 + 0.783i$	$-0.051 + 0.782i$	$-0.051 + 0.782i$
λ_9	$-0.052 - 0.783i$	$-0.051 - 0.782i$	$-0.051 - 0.782i$
λ_{10}	$-0.87 + 0i$	$-0.87 + 0i$	$-0.87 + 0i$
λ_{11}	$-0.22 + 0.452i$	$-0.22 + 0.452i$	$-0.22 + 0.452i$
λ_{12}	$-0.22 - 0.452i$	$-0.22 - 0.452i$	$-0.22 - 0.452i$
λ_{13}	$-0.024 + 0i$	$-0.024 + 0i$	$-0.024 + 0i$
λ_{14}	$-0.326 + 0i$	$-0.328 + 0i$	$-0.328 + 0i$
λ_{15}	$-0.564 + 0i$	$-0.564 + 0i$	$-0.564 + 0i$

also be investigated for its effect on system stability. The INEC method, as outlined in Section II-F, harnesses the energy held in the DC-link capacitors to modify the DC voltage and generate the active power supplied to the power system. Hence, it is crucial to assess the impact of the DC capacitance value on the stability of the system. Table 5 presents the eigenvalues for different DC-link capacitances. The results indicate that the eigenvalues are located on the left of the imaginary axis. However, there are no significant changes because the variations in the DC link voltage of the HVDC system are limited, and the stored energy in the DC link may not be enough to affect system stability.

V. SIMULATION
A. SIMULATION SETUP
A two-area interconnected system is presented in Fig. 1 used to evaluate the increasing RES effect on system frequency. The system includes four SGs with a rated capacity of 900 MW, together with an equivalent wind farm

TABLE 6. Simulation Scenarios.

Scenario	Description
1	A constant wind speed with sudden generation loss
2	A constant wind speed with sudden generation loss considering different droop coefficients of WT
3	Variable wind speeds and sudden generation loss

TABLE 7. Study cases in scenario 1.

Case	Description
1	No Control
2	HVDC Control
3	WT Control
4	HVDC+WT+BESS Control

with a capacity of 600 MW. The loads are located at buses 7 and 8, demanding a total active power of 2734 MW, including 976 MW in Area 1 and 1767 MW in Area 2. The specifications for SG can be seen in Section VI-A. Table 2 displays the characteristics of wind turbines.

The HVDC system in this work is positioned in parallel with the AC line, as shown in Fig. 1 and Fig. 5 [19], [21], [22]. The system comprises of two terminal VSC-HVDC converters, each with a rated capacity of 400 MW and a pole-to-pole rated DC link voltage of 300 kV. 400 MW of active power is expected to be transmitted from Area 1 to Area 2, which will utilize the HVDC link to transfer 200 MW of active power. The synchronization coefficient is further addressed in Section VI-B. The three scenarios, including a sudden generation loss combining different parameters and wind speed conditions, will be utilized to demonstrate the effectiveness and robustness of the proposed strategy. The detailed simulation scenarios are presented in Table 6.

B. SCENARIO 1: A CONSTANT WIND SPEED WITH SUDDEN GENERATION LOSS
A constant wind speed of $v_\omega = 10.5$ m/s (30% of wind power penetration) is considered in the first scenario. Four control strategies were used to demonstrate the effectiveness of the proposed LFC model and parameter, namely Case 1: without additional control, Case 2: with HVDC inertia control, Case 3: with WT inertia control, Case 4: HVDC+WT+BESS, as presented in Table 7. Fig. 13 illustrates the simulation results when Area 2 has a 0.08 pu generation outage at 10 s. Fig. 13(a) and (b) show the system frequency response in Areas 1 and 2, respectively. It is clearly seen that Case 4 uses simultaneous HVDC+WF+BESS, resulting in the frequency nadir being the highest among the four cases in both areas. The significant integration of wind turbines into the power
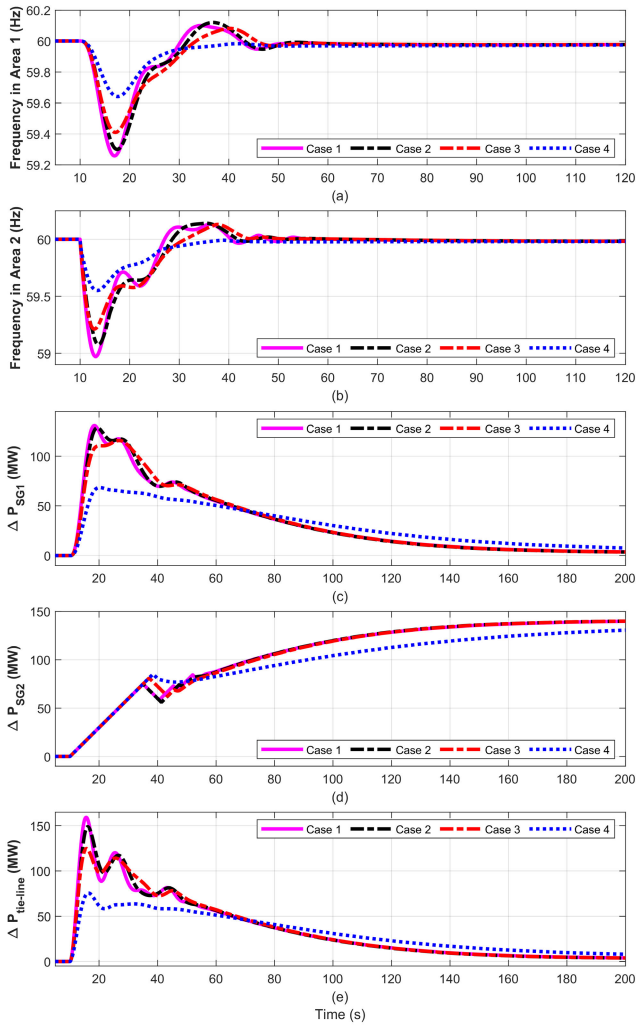
FIGURE 13. Simulation results of scenario 1. (a) System frequency in Area 1. (b) System frequency in Area 2. (c) Power deviation of SG in Area 1. (d) Power deviation of SG in Area 2. (e) Power deviation of tie-line.

FIGURE 14. Simulation results of scenario 1. (a) BESS power. (b) SOC. (c) Power deviation of HVDC. (d) DC-link voltage at HVDC. (e) Power deviation of WT. (f) Rotor speed.

system will lead to a decrease in system inertia. Consequently, without any further inertia support from external sources, the FN in Case 1 is the lowest compared to the other three scenarios. The energy stored in the limitation in the DC-link capacitor of HVDC leads to the frequency quality with inertia support by HVDC not significantly improving, as shown in Fig. 13(b). The additional active power by HVDC and its DC voltage participating in frequency regulation is shown in Fig. 14(c) and (c). In addition, by releasing the KE of WT, the amount of significant active power contributed to frequency regulation, as depicted in Fig. 14(e). As a result, the FN in Areas 1 and 2 has risen substantially. However, the substantial augmentation in the power of WT results in a notable reduction in rotor speed, which impacts the functioning of the WT. Therefore, the BESS is integrated to reduce the stress on WTs in Case 4. Specifically, a decrease in the rotor speed of WTs in Case 4 is improved compared to Case 3, as presented in Fig. 14(f). The active power of BESS
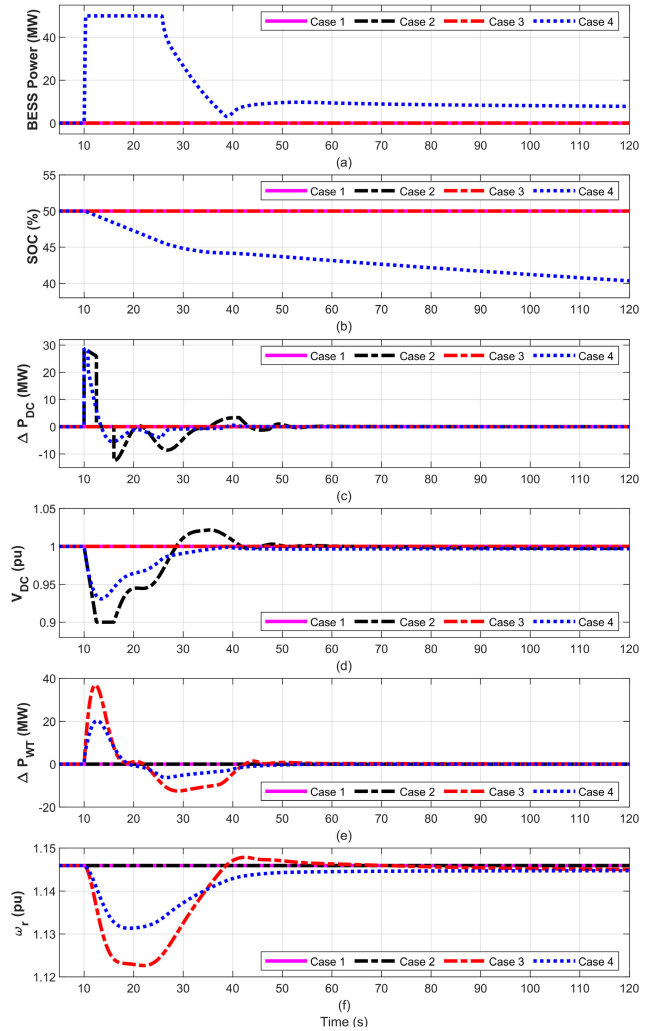
and its SOC are shown in Fig. 14(a) and (b). Notably, when detecting a frequency drop, the BESS can quickly ramp up its output power to the rating. Thereby, it directly helps SG in Area 1 in decreasing the active power sent on the tie-line to provide additional power for Area 2, leading to improved FN in Area 1. The change in mechanical power of SG in both areas are shown in Fig. 13(c) and (d).

C. SCENARIO 2: A CONSTANT WIND SPEED WITH SUDDEN GENERATION LOSS CONSIDERING DIFFERENT DROOP COEFFICIENT OF WT

This section aims to demonstrate the proposed strategy can fulfill different droop coefficients based on the system stability analysis in section III. b. Figs. 15 and 16 show the simulation results when Area 2 experiences a 0.08 p.u generation loss occurring at 10 s with a constant wind speed of 11.5 m/s. The system frequency in Areas 1 and 2 are illustrated in Fig. 15(a) and (b). It can be seen that the FN
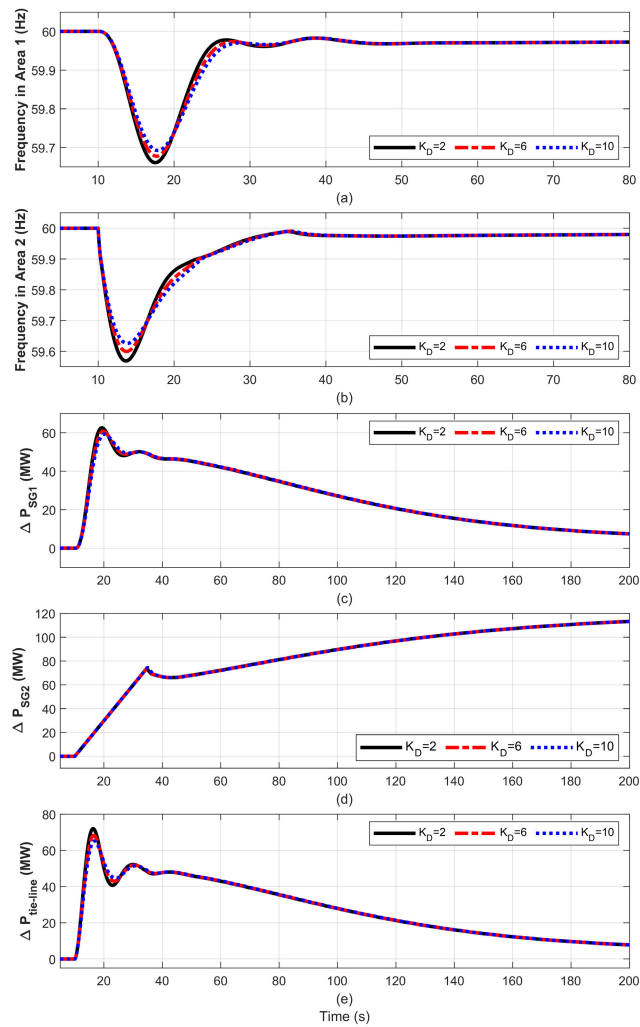
FIGURE 15. Simulation results of scenario 2. (a) System frequency in Area 1. (b) System frequency in Area 2. (c) Power deviation of SG in Area 1. (d) Power deviation of SG in Area 2. (e) Power deviation of tie-line.

FIGURE 16. Simulation results of scenario 2. (a) Power deviation of WT. (b) Rotor speed. (c) Captured wind power. (d) BESS power. (e) SOC.

in case $K_D = 10$ is the highest among all the cases. This is because, with $K_D = 10$, the WT can release more kinetic energy, which can be clearly observed in Fig. 16(a). However, the significant increase in the power of wind turbines leads to a noticeable decrease in rotor speed, as seen in Fig. 16(b). The outcomes indicate that the highest reduction in rotor speed occurs when the value of K_D is 10, followed by $K_D = 6$, and when K_D is 2, the impact on rotor speed is minimal. The reduction of rotor speed will reduce wind energy harvest. Fig. 16(c) displays the power reference generated by the MPPT algorithm once WT participates in a frequency regulation. The total wind energy loss associated with rotor speed recovery is quantified as the energy loss. The result indicates that the wind energy loss for rotor speed recovery is $S_1 = 0.2262$ p.u, $S_2 = 0.6782$ p.u, $S_1 = 1.13$ p.u, respectively. The change in mechanical power of SG in both areas are shown in Fig. 15(c) and (d). The active power of BESS and its SOC are shown in Fig. 16(d) and (e).
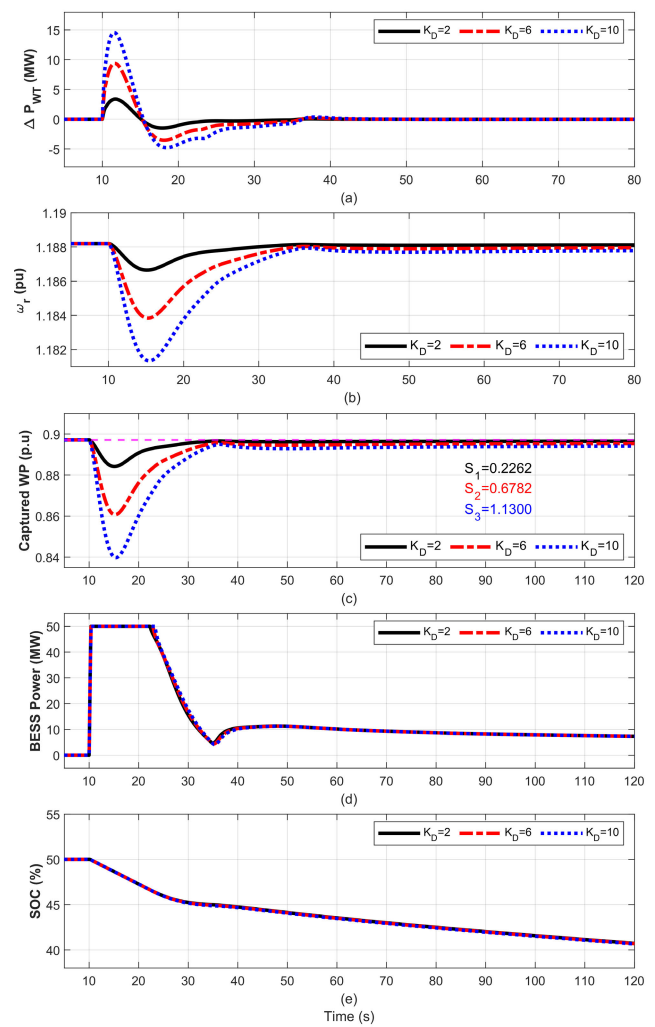
D. SCENARIO 3: VARIABLE WIND SPEEDS AND SUDDEN GENERATION LOSS

A variable wind-speed profile was designed to verify the effectiveness and robustness of the proposed strategy [37]. Fig. 17(a) depicts the wind-speed profile for this scenario. The initial wind speed is 11.5 m/s, gradually decreasing starting from the time at 10 s, while a sudden generation loss occurs in Area 2 at 40 s. At the initial stage, the wind speed decreases from 11.5 to 10.5 m/s, and the system frequency in both areas slightly declines. The SG, HVDC, and BESS collaborate to offer frequency control. After that, at 40 s, a sudden increasing load occurs, causing a significant decline in frequency. Fig. 18(b) indicates that the system frequency reaches the lowest value around 59.5 Hz in the case without WT control, while the FN is significantly improved when the participation of WT. This can be clearly seen in Fig. 17(b); the increasing output power of WT appears at the time of 40 s to participation in frequency regulation. In addition, the rising power of WT directly supports the SG in Area 1,
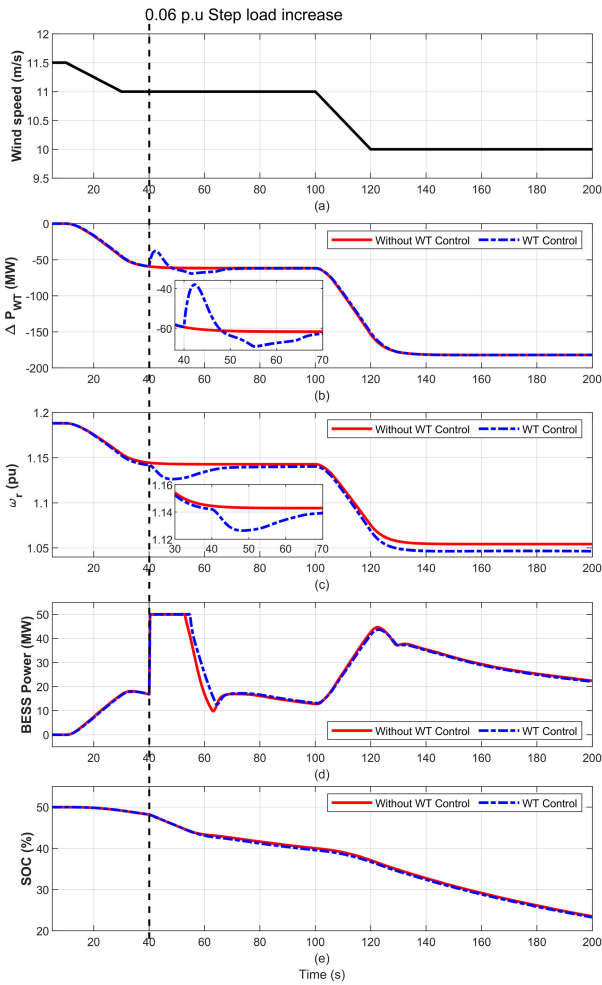
FIGURE 17. Simulation results of scenario 3. (a) Wind speed curve. (b) Power deviation of WT. (c) Rotor speed. (d) BESS power. (e) SOC.

FIGURE 18. Simulation results of scenario 3. (a) System frequency in Area 1. (b) System frequency in Area 2. (c) Power deviation of SG in Area 1. (d) Power deviation of SG in Area 2. (e) Power deviation of tie-line.

reducing the increasing power to support Area 2, as shown in Fig. 18(c). As a result, the frequency nadir in the case of WT joins to frequency regulation also improves in Area 1. Moreover, as depicted in Fig. 17(d), BESS can support a fast response to reduce the burden of SGs for supporting frequency regulation no matter how wind speeds change. Finally, the SOC of BESS is depicted in Fig. 17(e), where a stable operation of BESS is ensured during the entire simulation.

After three simulation scenarios, it can be concluded that the proposed coordinated strategy can fulfill different wind speeds and various disturbances. The simulation results from Scenario 2 indicate that the droop coefficient significantly impacts both the increase in output and the rotor speed recovery of the WT. In addition, Scenario 1 demonstrates that with a high integration of RES into the power grid, incorporating diverse sources such as HVDC, WF, and BESS to support SGs in frequency regulation can enhance the FN, and improve frequency stability.
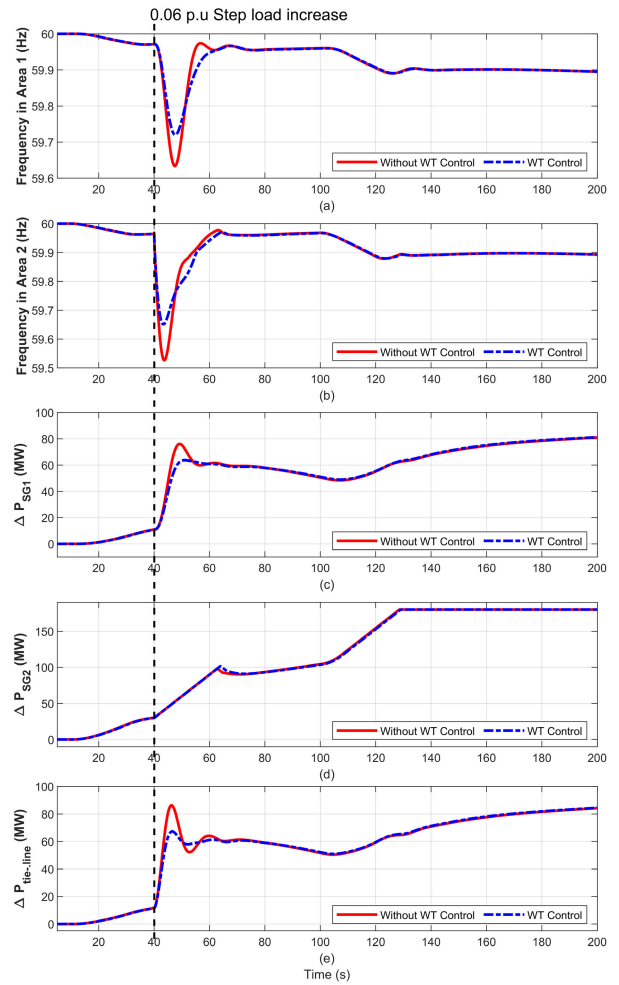
VI. CONCLUSION

A novel LFC model coordinating control among HVDC, WF, BESS, and SG has been proposed in this work to address the limitations of existing studies. These existing studies mainly used simplified first-order transfer functions of WT, BESS, and HVDC to obtain the parameters of supplementary control for SGs. The proposed strategy establishes a comprehensive state-space model, including all the dynamic models and their control strategies of the BESS, WT, HVDC, and SG within the LFC model. From the state-space model, the control parameters used in the LFC strategy, such as the droop coefficient of the BESS strategy, the influence of wind speeds on the WT, different virtual inertia coefficients, the variation in the droop coefficient of the WT control, and the impact of the DC capacitance in the HVDC control strategy, were investigated for their effect on system stability. The investigation concerning about the coefficient impact of frequency regulation on system stability yielded a specific range of coefficients to guarantee stability for the

studied system. According to the recommended parameters, the outcomes reveal that with a high penetration of RES into the power grid, the proposed strategy can improve frequency stability. Additionally, the results indicate that incorporating diverse sources such as HVDC, WF, and BESS to support SGs in frequency regulation improves the problem of low system inertia, leading to an FN that is higher not only in the area where disturbances occur but also in other areas when tie-line power interchanges are maintained in balance. Moreover, the proposed strategy demonstrates that it still performs well with load changes under wind speed changes. However, this study mainly concentrates on determining BESS specifications based on specific technical power requirements without incorporating economic analysis. Future research will integrate identifying the optimal size of BESS installations with economic analyses, stability analysis, and the application of a customized algorithm for fine-tuning the relevant variables.

APPENDIX
A. NOMINAL PARAMETERS FOR TWO-AREA INTERCONNECTED SYSTEM
$P_1 = P_2 = 1800$ MW, $P_{tie,AC_{max}} = 400$ MW, $P_{tie,DC_{max}} = 400$ MW, $f_0 = 60$ Hz, $H_1 = 6$ MWs/MVA, $H_2 = 4$ MWs/MVA, $D_1 = D_1 = 8.33 * 10^{-3}$ puMW/Hz, $R_1 = R_2 = 2.4$ Hz/puMW.

B. SYNCHRONIZATION COEFFICIENT CALCULATIONS
1) AC SYNCHRONIZATION COEFFICIENT CALCULATIONS
The maximum power transfer capability of the AC line is $P_{max,AC} = 400$ MW. The rated capacity of area 1 is

$P_1 = 1800$ MW. In this work, the loading of the AC line is considered 50%. Therefore, the AC synchronization coefficient is $T_{AC} = 0.1925$.

2) DC SYNCHRONIZATION COEFFICIENT CALCULATIONS
The maximum power transfer capability of the DC line is $P_{max,DC} = 200$ MW. The rated capacity of area 1 is $P_1 = 2000$ MW, and area 2 is $P_2 = 2000$ MW. This work considers the DC line loading to be 50%. Hence, the equivalent DC synchronization coefficient is $T_{DC} = 0.09625$.

C. STATE SPACE MODEL MATRICES
For a two-area restructured power system model interconnected via hybrid AC/DC, the system matrix A is of the order of 15×15, and its non-zero (a_{ij}) elements are given as:

$$a_{1,1} = \frac{-D_1}{2H_1}, a_{1,2} = \frac{1}{2H_1}, a_{1,6} = -\frac{1}{2H_1};$$

$$a_{2,1} = \frac{2R_P}{T_{G1}R_T R_1}, a_{2,2} = -\frac{2}{T_w}, a_{2,3} = \frac{2R_P(T_R - T_{G1})}{R_T T_R T_{G1}},$$

$$a_{2,4} = \frac{2}{T_w} + \frac{2R_P}{R_T T_R};$$

$$a_{3,1} = -\frac{1}{R_1 T_{G1}}, a_{3,3} = -\frac{1}{T_{G1}};$$

$$a_{4,1} = -\frac{R_P}{T_{G1}R_T R_1}, a_{4,3} = \frac{R_P(T_{G1} - T_R)}{R_T T_R T_{G1}}, a_{4,4} = -\frac{R_P}{R_T T_R}$$

$$a_{5,5} = -\frac{1}{T_{ESS}}, a_{5,7} = \frac{K_{ESS}}{T_{ESS}}$$

$$A = \begin{bmatrix}
a_{1,1} & a_{1,2} & 0 & 0 & 0 & a_{1,6} & 0 & 0 & 0 & 0 & 0 & 0 & 0 & 0 & 0 \\
a_{2,1} & a_{2,2} & a_{2,3} & a_{2,4} & 0 & 0 & 0 & 0 & 0 & 0 & 0 & 0 & 0 & 0 & 0 \\
a_{3,1} & 0 & a_{3,3} & 0 & 0 & 0 & 0 & 0 & 0 & 0 & 0 & 0 & 0 & 0 & 0 \\
a_{4,1} & 0 & a_{4,3} & a_{4,4} & 0 & 0 & 0 & 0 & 0 & 0 & 0 & 0 & 0 & 0 & 0 \\
0 & 0 & 0 & 0 & a_{5,5} & 0 & a_{5,7} & 0 & 0 & 0 & 0 & 0 & 0 & 0 & 0 \\
a_{6,1} & 0 & 0 & 0 & 0 & a_{6,7} & 0 & 0 & 0 & 0 & 0 & 0 & 0 & 0 & 0 \\
0 & 0 & 0 & 0 & a_{7,5} & a_{7,6} & a_{7,7} & a_{7,8} & 0 & 0 & 0 & 0 & a_{7,13} & a_{7,14} & 0 \\
0 & 0 & 0 & 0 & 0 & 0 & 0 & a_{8,8} & a_{8,9} & a_{8,10} & 0 & 0 & 0 & 0 & 0 \\
0 & 0 & 0 & 0 & 0 & 0 & a_{9,7} & 0 & a_{9,9} & 0 & 0 & 0 & 0 & 0 & 0 \\
0 & 0 & 0 & 0 & 0 & 0 & 0 & 0 & a_{10,9} & a_{10,10} & 0 & 0 & 0 & 0 & 0 \\
a_{11,1} & 0 & 0 & 0 & 0 & a_{11,6} & a_{11,7} & 0 & 0 & 0 & 0 & 0 & 0 & 0 & 0 \\
0 & 0 & 0 & 0 & 0 & a_{12,6} & a_{12,7} & 0 & 0 & 0 & 0 & 0 & 0 & 0 & 0 \\
0 & 0 & 0 & 0 & 0 & 0 & 0 & 0 & 0 & 0 & 0 & 0 & a_{13,13} & a_{13,14} & 0 \\
0 & 0 & 0 & 0 & 0 & 0 & 0 & 0 & 0 & 0 & 0 & 0 & 0 & a_{14,14} & a_{14,15} \\
0 & 0 & 0 & 0 & a_{15,5} & a_{15,6} & a_{15,7} & a_{15,8} & 0 & 0 & 0 & 0 & a_{15,13} & a_{15,14} & a_{15,15}
\end{bmatrix} \quad (39)$$

$$a_{6,1} = 2\pi (T_{DC} + T_{AC}), a_{6,7} = -2\pi (T_{DC} + T_{AC});$$

$$a_{7,5} = -\frac{1}{2H_2}, a_{7,6} = \frac{1}{2H_2}, a_{7,7} = -\frac{D_2}{2H_2}$$
$$- \frac{H_{VSC}S_{VSC}I_{DC}}{NC_{DC}f_0 V_{DC0}^2} \frac{1}{2H_2},$$

$$a_{7,8} = \frac{1}{2H_2}, a_{7,13} = \frac{X_2 P_{WT0}}{2H_2}, a_{7,14} = \frac{X_2 \omega_{r0}}{2H_2};$$

$$a_{8,8} = -\frac{1}{T_{RH}}, a_{8,9} = \frac{F_{HP}}{T_{CH}}, a_{8,10} = \frac{1}{T_{RH}} - \frac{F_{HP}}{T_{CH}};$$

$$a_{9,7} = -\frac{1}{R_2 T_{G2}}, a_{9,9} = -\frac{1}{T_{G2}};$$

$$a_{10,9} = \frac{1}{T_{CH}}, a_{10,10} = -\frac{1}{T_{CH}};$$

$$a_{11,1} = B_1, a_{11,6} = 1, a_{11,7} = \frac{2H_{VSC}S_{VSC}I_{DC}}{NC_{DC}f_0 V_{DC0}^2};$$

$$a_{12,6} = -1, a_{12,7} = B_2 - \frac{2H_{VSC}S_{VSC}I_{DC}}{NC_{DC}f_0 V_{DC0}^2};$$

$$a_{13,13} = \frac{\tau_1}{2H_{WT}}, a_{13,14} = -\frac{X_3}{2H_{WT}};$$

$$a_{14,14} = -\frac{1}{T_1}, a_{14,15} = \frac{X_2}{T_1};$$

$$a_{15,5} = \frac{K_D X_1 K_{p\omega}}{2H_2 \omega_{r0}}, a_{15,6} = -\frac{K_D X_1 k_{p,\omega}}{2H_2 \omega_{r0}}, a_{15,7} = -\frac{K_D X_1 k_{p,\omega} D_2}{2H_2 \omega_{r0}} + \frac{K_D X_1 k_{p,\omega}}{2H_2 \omega_{r0}} \frac{2H_{VSC}S_{VSC}I_{DC}}{NC_{DC}f_0 V_{DC0}^2} - \frac{K_D X_1 k_{i,\omega}}{\omega_{r0}}, a_{15,8} = -\frac{K_D X_1 k_{p,\omega}}{2H_2 \omega_{r0}}, a_{15,13} = \frac{3K_{opt} \omega_{r0} X_1 k_{p,\omega} \tau_1}{2H_{WT}} - \frac{K_D X_1 k_{p,\omega} X_3 i_{qs0}}{2H_2 \omega_{r0}} + 3K_{opt} \omega_{r0} X_1 k_{i,\omega}, a_{15,14} = \frac{3K_{opt} \omega_{r0} X_1 k_{p,\omega} X_3}{2H_{WT}} - \frac{K_D X_1 k_{p,\omega} X_3 \omega_{r0}}{2H_2 \omega_{r0}} + \frac{k_{p,\omega}}{T_1} - k_{i,\omega}, a_{15,15} = -\frac{k_{p,\omega} X_2}{T_1},$$

(39) as shown at the bottom of the previous page.

REFERENCES

[1] M. Mehrabankhomartash, M. Saeedifard, and A. Yazdani, "Adjustable wind farm frequency support through multi-terminal HVDC grids," *IEEE Trans. Sustain. Energy*, vol. 12, no. 2, pp. 1461–1472, Apr. 2021.

[2] D.-T. Trinh, Y.-K. Wu, and M.-H. Pham, "Adaptive frequency control strategy for PMSG-based wind turbines with improved rotor speed recovery," *IEEE Access*, vol. 12, pp. 63853–63864, 2024.

[3] C.-H. Lin and Y.-K. Wu, "Coordinated frequency control strategy for VSC-HVDC-connected wind farm and battery energy storage system," *IEEE Trans. Ind. Appl.*, vol. 59, no. 5, pp. 5314–5328, Sep. 2023.

[4] Y.-L. Hu and Y.-K. Wu, "Inertial response identification algorithm for the development of dynamic equivalent model of DFIG-based wind power plant," *IEEE Trans. Ind. Appl.*, vol. 57, no. 3, pp. 2104–2113, May 2021.

[5] Y. Wang, Z. Wang, J. Gan, H. Zhang, and R. Wang, "Switched observer-based adaptive event-triggered load frequency control for networked power systems under aperiodic DoS attacks," *IEEE Trans. Smart Grid*, vol. 14, no. 6, pp. 4816–4826, Nov. 2023.

[6] Y. Wang, Y. Liu, X. Yu, and H. Zhang, "Jointed observer-based sliding mode predictive control for interconnected power systems with input delays," *IEEE Trans. Autom. Sci. Eng.*, early access, Jan. 25, 2024, doi: 10.1109/TASE.2024.3353166.

[7] H. Gozde and M. C. Taplamacioglu, "Automatic generation control application with craziness based particle swarm optimization in a thermal power system," *Int. J. Electr. Power Energy Syst.*, vol. 33, no. 1, pp. 8–16, Jan. 2011.

[8] E. S. Ali and S. M. Abd-Elazim, "Bacteria foraging optimization algorithm based load frequency controller for interconnected power system," *Int. J. Electr. Power Energy Syst.*, vol. 33, no. 3, pp. 633–638, Mar. 2011.

[9] C. K. Shiva, G. Shankar, and V. Mukherjee, "Automatic generation control of power system using a novel quasi-oppositional harmony search algorithm," *Int. J. Electr. Power Energy Syst.*, vol. 73, pp. 787–804, Dec. 2015.

[10] D. Guha, P. K. Roy, and S. Banerjee, "Load frequency control of large scale power system using quasi-oppositional grey wolf optimization algorithm," *Eng. Sci. Technol., Int. J.*, vol. 19, no. 4, pp. 1693–1713, Dec. 2016.

[11] P. Dash, L. C. Saikia, and N. Sinha, "Automatic generation control of multi area thermal system using bat algorithm optimized PD-PID cascade controller," *Int. J. Electr. Power Energy Syst.*, vol. 68, pp. 364–372, Jun. 2015.

[12] H. Wang and Z. S. Li, "Multi-area load frequency control in power system integrated with wind farms using fuzzy generalized predictive control method," *IEEE Trans. Rel.*, vol. 72, no. 2, pp. 737–747, Jun. 2023.

[13] X. Li and D. Ye, "Event-based distributed fuzzy load frequency control for multiarea nonlinear power systems with switching topology," *IEEE Trans. Fuzzy Syst.*, vol. 30, no. 10, pp. 4262–4272, Oct. 2022.

[14] A. Elmelegi, E. A. Mohamed, M. Aly, E. M. Ahmed, A. A. Mohamed, and O. Elbaksawi, "Optimized tilt fractional order cooperative controllers for preserving frequency stability in renewable energy-based power systems," *IEEE Access*, vol. 9, pp. 8261–8277, 2021.

[15] S. Trip, M. Cucuzzella, C. De Persis, A. van der Schaft, and A. Ferrara, "Passivity-based design of sliding modes for optimal load frequency control," *IEEE Trans. Control Syst. Technol.*, vol. 27, no. 5, pp. 1893–1906, Sep. 2019.

[16] D. Rerkpreedapong, A. Hasanovic, and A. Feliachi, "Robust load frequency control using genetic algorithms and linear matrix inequalities," *IEEE Trans. Power Syst.*, vol. 18, no. 2, pp. 855–861, May 2003.

[17] N. Vafamand, M. M. Arefi, M. H. Asemani, and T. Dragicevic, "Decentralized robust disturbance-observer based LFC of interconnected systems," *IEEE Trans. Ind. Electron.*, vol. 69, no. 5, pp. 4814–4823, May 2022.

[18] B. K. Sahu, T. K. Pati, J. R. Nayak, S. Panda, and S. K. Kar, "A novel hybrid LUS-TLBO optimized fuzzy-PID controller for load frequency control of multi-source power system," *Int. J. Electr. Power Energy Syst.*, vol. 74, pp. 58–69, Jan. 2016.

[19] Y. Arya and N. Kumar, "AGC of a multi-area multi-source hydrothermal power system interconnected via AC/DC parallel links under deregulated environment," *Int. J. Electr. Power Energy Syst.*, vol. 75, pp. 127–138, Feb. 2016.

[20] E. Sahin, "Design of an optimized fractional high order differential feedback controller for load frequency control of a multi-area multi-source power system with nonlinearity," *IEEE Access*, vol. 8, pp. 12327–12342, 2020.

[21] N. Pathak, A. Verma, T. S. Bhatti, and I. Nasiruddin, "Modeling of HVDC tie links and their utilization in AGC/LFC operations of multiarea power systems," *IEEE Trans. Ind. Electron.*, vol. 66, no. 3, pp. 2185–2197, Mar. 2019.

[22] E. Rakhshani and P. Rodriguez, "Inertia emulation in AC/DC interconnected power systems using derivative technique considering frequency measurement effects," *IEEE Trans. Power Syst.*, vol. 32, no. 5, pp. 3338–3351, Sep. 2017.

[23] T. H. Mohamed, J. Morel, H. Bevrani, and T. Hiyama, "Model predictive based load frequency control design concerning wind turbines," *Int. J. Electr. Power Energy Syst.*, vol. 43, no. 1, pp. 859–867, Dec. 2012.

[24] N. Nguyen and J. Mitra, "An analysis of the effects and dependency of wind power penetration on system frequency regulation," *IEEE Trans. Sustain. Energy*, vol. 7, no. 1, pp. 354–363, Jan. 2016.

[25] G. Magdy, H. Ali, and D. Xu, "Effective control of smart hybrid power systems: Cooperation of robust LFC and virtual inertia control system," *CSEE J. Power Energy Syst.*, vol. 8, no. 6, pp. 1583–1593, Nov. 2021.

[26] J. Cao, W. Du, H. Wang, and M. McCulloch, "Optimal sizing and control strategies for hybrid storage system as limited by grid frequency deviations," *IEEE Trans. Power Syst.*, vol. 33, no. 5, pp. 5486–5495, Sep. 2018.

[27] B.-K. Chiu, K.-Y. Lee, and Y.-Y. Hsu, "Battery energy storage system damper design for a microgrid with wind generators participating in frequency regulation," *Energies*, vol. 16, no. 21, p. 7439, Nov. 2023.

[28] P. Kundur, *Power System Stability and Control*. New York, NY, USA: McGraw-Hill, 1994.

[29] E. Rakhshani and P. Rodriguez, "Active power and frequency control considering large-scale RES," in *Large Scale Renewable Power Generation*, J. Hossain and A. Mahmud, Eds., Singapore: Springer, 2014, pp. 233–271.

[30] Y. Ota, H. Taniguchi, T. Nakajima, K. M. Liyanage, J. Baba, and A. Yokoyama, "Autonomous distributed V2G (vehicle-to-grid) satisfying scheduled charging," *IEEE Trans. Smart Grid*, vol. 3, no. 1, pp. 559–564, Mar. 2012.

[31] J. B. Ekanayake, N. Jenkins, and G. Strbac, "Frequency response from wind turbines," *Wind Eng.*, vol. 32, no. 6, pp. 573–586, Dec. 2008.

[32] M. Toulabi, S. Bahrami, and A. M. Ranjbar, "An input-to-state stability approach to inertial frequency response analysis of doubly-fed induction generator-based wind turbines," *IEEE Trans. Energy Convers.*, vol. 32, no. 4, pp. 1418–1431, Dec. 2017.

[33] M. Toulabi, A. S. Dobakhshari, and A. M. Ranjbar, "An adaptive feedback linearization approach to inertial frequency response of wind turbines," *IEEE Trans. Sustain. Energy*, vol. 8, no. 3, pp. 916–926, Jul. 2017.

[34] C.-H. Lin and Y.-K. Wu, "Overview of frequency-control technologies for a VSC-HVDC-integrated wind farm," *IEEE Access*, vol. 9, pp. 112893–112921, 2021.

[35] L. Meng, J. Zafar, S. K. Khadem, A. Collinson, K. C. Murchie, F. Coffele, and G. M. Burt, "Fast frequency response from energy storage systems—A review of grid standards, projects and technical issues," *IEEE Trans. Smart Grid*, vol. 11, no. 2, pp. 1566–1581, Mar. 2020.

[36] V. Knap, S. K. Chaudhary, D.-I. Stroe, M. Swierczynski, B.-I. Craciun, and R. Teodorescu, "Sizing of an energy storage system for grid inertial response and primary frequency reserve," *IEEE Trans. Power Syst.*, vol. 31, no. 5, pp. 3447–3456, Sep. 2016.

[37] Z. Zhao, X. Luo, J. Xie, S. Gong, J. Guo, Q. Ni, C. S. Lai, P. Yang, L. L. Lai, and J. M. Guerrero, "Decentralized grid-forming control strategy and dynamic characteristics analysis of high-penetration wind power microgrids," *IEEE Trans. Sustain. Energy*, vol. 13, no. 4, pp. 2211–2225, Oct. 2022.

YUAN-KANG WU (Member, IEEE) received the Ph.D. degree in electronic and electrical engineering from the University of Strathclyde, Glasgow, U.K., in 2004.

He was a Researcher with the Industrial Technology Research Institute, Hsinchu, Taiwan, and an Engineer with Taiwan Electric Research and Testing Center, Taiwan. He is currently a Professor with the Department of Electrical Engineering, National Chung Cheng University, Chiayi, Taiwan, involved in the area of wind turbine modeling, wind and solar power systems, offshore wind farm planning, renewable energy forecasting techniques, power system control and management, distributed generation, and smart grid control. He is also the Technical Committee Program Chair of the Energy Systems Committee of Industry Application Society of IEEE and an Associate Editor of IEEE Transactions on Industry Applications.

DUC-TUNG TRINH (Graduate Student Member, IEEE) received the B.S. degree in electrical engineering from Hanoi University of Science and Technology (HUST), Vietnam, in 2021. He is currently pursuing the M.S degree with National Chung Cheng University.

His research interests include inverter-based resources grid-forming, wind turbine modeling, and control.

MANH-HAI PHAM (Member, IEEE) was born in Hải Dương, Vietnam, in 1983. He received the B.S. degree in power system from Hanoi University of Science and Technology, in 2006, the M.S. degree in power system from the University of Paul Sabatier, Toulouse, France, in 2008, and the Ph.D. degree in plasma applications from the University of Poitiers, Poitiers, France, in 2011.

Since 2012, he has been a Lecturer with Electric Power University, Hanoi, Vietnam. His research interests include load forecasting, stability, reliability of power systems, renewable energy, and nonthermal plasma discharge processes and applications.

● ● ●